New Airborne Thermal-Infrared Hyperspectral Imager System: Initial Validation

Chengyu Liu , Rui Xu, Feng Xie, Jian Jin, Liyin Yuan, Gang Lv, Yueming Wang , Chunlai Li ,
and Jianyu Wang

Abstract—**Compared with hyperspectral remote sensing in visible-light, near infrared and short-wave infrared spectra, hyperspectral remote sensing in the thermal infrared spectrum has unique advantages, especially in the fields of mineral identification and pollution gas. At present, infrared hyperspectral imagers are rare and mainly airborne. In this article, the basic principle and design features of a newly developed airborne thermal-infrared hyperspectral imaging system (ATHIS) are detailed, and separate validation experiments of laboratory and aerial remote sensing experiments are carried out. Measurements and comparative analysis of infrared emissivity spectra of the typical minerals were performed in the laboratory. In the summer of 2019, the instrument carried out flight tests in Hengdian Town, Dongyang City, Zhejiang Province, China. The results show that ATHIS can also accurately acquire the target emissivity spectrum. In the future, the instrument will also be used to carry out key technology verification and data-processing application research of space infrared hyperspectral imagers plan.**

Index Terms—**Cryogenic optics, focal plane assembly, infrared hyperspectral sensors, spectral resolution, temperature and emissivity inversion.**

I. Introduction

IN THE field of infrared Earth observation, obtaining the land surface temperature (LST) and land surface emissivity is a prerequisite for the characteristic identification of ground objects in the real world. At present, many assumptions and much prior knowledge are needed to acquire ground temperature from the traditional single-band, dual-band, or multiband infrared imaging technologies. From the perspective of infrared remote sensing, the actual LST must be obtained through the accurate separation of physical temperature and emissivity. Reducing the use of hypothetical prerequisites and prior knowledge is the only way to retrieve the ground surface temperature and emissivity objectively and accurately. Thermal infrared (TIR) hyperspectral imaging technology provides a new remote-sensing technology for achieving the aforementioned goals.

Based on a similar principle in traditional visible or near-infrared imaging spectrometers, a TIR hyperspectral imager mainly obtains the fine spectrum and image information of the $(8–12.5)$-μm spectrum. The sharp increase in the number of bands is conducive to reducing the assumptions needed in the separation of temperature and emissivity. Through the characteristics of the emissivity spectrum, the number of unknowns in the TIR radiation transfer equations can be reduced, which makes the ill-posed problem more well-posed, and then more accurate temperature and emissivity can be obtained. Based on this, study of the TIR hyperspectral remote sensing can play an important role in Earth climate change, urban heat island and cold island effects, the remote-sensing drought index, earthquake infrared radiation, atmospheric environment monitoring, and other fields.

Different from the hyperspectral imagers in visible and short-wave infrared spectra, the development of which is focused on the light-splitting module and detector [1], development of infrared hyperspectral imagers is mainly concerned with suppressing infrared background radiation [2], [3]. A spatially enhanced broadband array spectrograph system (SEBASS) was developed by Aerospace Corporation in 1996 [4]. A set of low-temperature optical systems with all-optical-circuit refrigeration was designed for the instrument. The entire system is cooled to 10 K by liquid helium to reduce the influence of the background radiation of the light machine and improve the overall performance of the instrument. In 1998, an airborne infrared hyperspectral imager (AHI) was successfully developed at the University of Hawaii [5]. The instrument uses the cooling gradient filter inlaid on the focal plane surface to suppress the background radiation and the plane grating for the light splitting. The spectrometer of the AHI system does not use low-temperature optical refrigeration, so it has 32 bands and the spectral resolution is approximately 125 nm. In the follow-up development of the AHI, researchers at the University of Hawaii used Stirling refrigeration to reduce the temperature and further reduce the background radiation. In 2003, a long-wave hyperspectral imaging spectrometer was developed by the Northrop Grumman Space Technology [6]. To suppress the background radiation, the entire system is installed in the vacuum chamber with gold plating on the surface, and the optical–mechanical system is cooled to below 100 K. The

Chengyu Liu, Rui Xu, Feng Xie, Jian Jin, Liyin Yuan, Gang Lv, and Yueming Wang are with the Key Laboratory of Space Active Opto-Electronics Technology, the Shanghai Institute of Technical Physics, Chinese Academy of Sciences, Shanghai 200083, China (e-mail: chengyuliu@vip.qq.com; xurui@mail.sitp.ac.cn; xf@mail.sitp.ac.cn; jinjian@mail.sitp.ac.cn; yuanliyintongji@mail.sitp.ac.cn; lvgang@mail.sitp.ac.cn; wangym@mail.sitp.ac.cn).

Chunlai Li and Jianyu Wang are with the Key Laboratory of Space Active Opto-Electronics Technology, the Shanghai Institute of Technical Physics, Chinese Academy of Sciences, Shanghai 200083, China, and with University of Chinese Academy of Sciences, Beijing 100049, China, and also with the Hangzhou Institute for Advanced Study, the University of Chinese Academy of Sciences, Hangzhou 310024, China (e-mail: lichunlai@mail.sitp.ac.cn; jywang@mail.sitp.ac.cn).

spectrometer uses a plane grating to divide the light with 128 spectral bands. The instrument also has an on-board real-time calibration device. Actual validation shows that the absolute radiometric calibration accuracy is better than 6%. On the basis of the SEBASS, two other high-performance long-wave infrared hyperspectral imagers, MAKO and MAGI, were developed by Aerospace Corporation [7], [8]. Compared with the SEBASS, the performance of MAKO is greatly improved. The spectral range of MAKO is 7.8–13.4 μm, and the number of channels is 128. To adapt to the imaging of the silicon detector, the entire spectrometer is cooled to approximately 10 K. MAGI has only 32 wavebands, which is equivalent to the optimized version of MAKO. It is, in essence, a predeveloped prototype of the on-board TIR hyperspectral imager. MAGI uses Stirling refrigeration to suppress background radiation and HgCdTe for the focal plane array (FPA). In 2011, the Defense Procurement Agency entrusted Onera, the French aerospace laboratory, to develop an infrared imaging spectrometer, including medium-wave infrared (3–5.3 μm) and long-wave infrared (8–11.5 μm), called SIELETERS [9]. With Fourier-transform imaging and liquid-nitrogen refrigeration, the spectral resolution of SIELETERS is better than 13 cm^{-1} in medium-wave infrared and 6 cm^{-1} in long-wave infrared. In 2010, workers at NASA's Jet Propulsion Laboratory (JPL) began to use the infrared spectrometer (including slit and detector) scheme of low-temperature optical refrigeration. The refrigeration temperature is near 40 K and the telescope is designed to work at normal temperature. The advantage of this scheme is that the spectrometer that needs refrigeration can be designed very precisely, so as to reduce the volume and complexity of the instrument. HyTES, an airborne TIR hyperspectral imager developed by JPL in 2013, adopts a similar scheme and represents the highest level of the development of the TIR hyperspectral imager [10]. Its technical difficulty even exceeds most of the space hyperspectral imagers in the same period [3].

All of the aforementioned instruments are one-of-a-kind research instruments developed by research institutions and companies, primarily for experimental research. Some companies have also launched their own commercial infrared imaging spectrometers, mainly, e.g., TASI-600 [11], AISA OWL,[1] and Hyper-Cam [12]. In 2006, Canadian ITRES Research Limited released the first commercial infrared hyperspectral imager, TASI-600. It has 32 bands in the (8–11.5)-μm spectral range. To reduce the weight and volume, the optical design of TASI was optimized and the MCT detector with low-temperature refrigeration adopted. The mass of TASI is only 40 kg. AISA OWL is an infrared hyperspectral imager developed by Finland's Specim company. It has 96 bands in the spectral range of 7.7–12.5 μm, and its spectral resolution is 100 nm. A cooled HgCdTe array detector is adopted in AISA OWL. The background radiation of the instrument is suppressed by special filter technology, and the background monitoring and correction function is added to the chip. With a total field of view (FOV) of 40°, it weighs only 13.1 kg and its volume is only 17.5 $\times$ 28.5 $\times$ 20 cm^3, which make it possible to be installed on a very small airborne platform. Hyper-Cam is a Fourier-transform TIR hyperspectral imager

developed by Telops of Canada. Hyper-Cam has two models, hyper-cam MW (3–5 μm) and hyper-cam LW (7.7–11.8 μm). The spectrum range of the latest version, Hyper-Cam XLW, is 7.35–13.5 μm. Hyper-Cam has high spatial resolution and spectral resolution. Its spatial resolution is 0.35 mrad and its spectral resolution is better than 0.25 cm^{-1}. However, its field angle is relatively small, only 6.1° $\times$ 5.1°.

In the development process of infrared imaging spectrometers, in order to reduce the overall volume and mass of the instrument as much as possible, background radiation suppression has developed from whole-instrument refrigeration to partial refrigeration. The refrigeration mode has also gradually changed from nitrogen to Stirling type. In addition, a large FOV is also a necessary configuration. In this article, an airborne thermal-infrared hyperspectral imaging system (ATHIS) is introduced, and laboratory measurement and aerial remote-sensing experiments carried out for the instrument. The method of retrieving the surface temperature and emissivity from the data is also given. The retrieved emissivity spectrum was compared with the emissivity spectrum measured synchronously by a commercial Fourier-transform infrared spectrometer and the emissivity spectrum in the spectral library. Through these experiments, the performance of the instrument is preliminarily demonstrated, and a reference for further application in the future is also provided.

II. GENERAL DESIGN OF ATHIS

A. Design Specifications

ATHIS is deployed on an aerial platform and its instantaneous FOV corresponds to the infrared hyperspectral information of a line on the ground. The hyperspectral data cube of the ground is obtained through the movement of the platform. ATHIS adopts the technical scheme of spectrometer refrigeration, and the refrigeration temperature is 100 K. The instrument uses a planar diffraction grating [13]. To improve the data-acquisition efficiency, three cameras (each 14°) are used to achieve the FOV of 40°. Table I presents a comparison between the characteristics of ATHIS and several typical instruments in use around the world. The metrics of ATHIS are basically the same as those of HyTES, except for the spectral resolution. HyTES is being developed to support the hyperspectral infrared imager (HyspIRI) mission and it provides the HyspIRI group data at much higher spatial and spectral resolutions to help determine the optimum band positions for the HyspIRI-TIR instrument. Additionally, it provides precursor datasets for Earth science research in the TIR.[2]

For ATHIS, the further improvement of the spectral resolution is primarily limited by the dark current of the infrared FPA. The signal introduced by the dark current when the instrument is exposed to the infrared energy of the target for a long time occupies the dynamic range.

B. System Composition

Three identical TIR hyperspectral cameras are used to achieve 40° observation FOV by postmosaic and the FOV of a single camera is approximately 14°. To reduce the volume of ATHIS,

---

[1][Online]. Available: https://www.specim.fi/products/aisaowl/

[2][Online]. Available: https://hytes.jpl.nasa.gov/

TABLE I
INSTRUMENT CHARACTERISTICS OF TYPICAL AIRBORNE HYPERSPECTRAL LONG-WAVE TIR SYSTEMS

Instrument	Spectral range (μm)	Spectral resolution (nm)	Bands	IFOV (mrad)	Sensitivity	Spectral-splitting	Background radiation suppression
SEBASS	7.6-13.5	46 nm	128	1.1	0.05 K	Curved prism	The entire optical circuit is cooled by liquid helium, and the detector is cooled to 10K
AHI	7.5-11.5	125 nm	32	2	0.1 K	Planar grating	The background suppressor is designed. Cold Lyot stop, linear variable filter and detector are cooled to 56K. The optics is cooled to 100K.
MAKO	7.8-13.4	47 nm	128	2	0.05 K	Concave grating	Spectrometer refrigeration(40 K)
AISA-OWL	7.7-12.3	100 nm	96	1.1	20 mW/(m^2·sr·μm)	P-G-P	Stirling cycle cooler
HyTES	7.5-12.0	18 nm	256	1.7	0.2 K	Concave grating	Spectrometer refrigeration(40 K)
Hyper-Cam	7.7-11.8	>0.25 cm^{-1}	256	0.35	20 nW/(cm^2·sr·cm^{-1})	Fourier transform	Fourier spectroscopy without low temperature optics
ATHIS	8-12.5	38 nm	155	1	0.17 K	Planar grating	Spectrometer refrigeration(100 K)

Fig. 1.   Composition of ATHIS.

Fig. 2.   Structure of RT spectrometer in a single module.
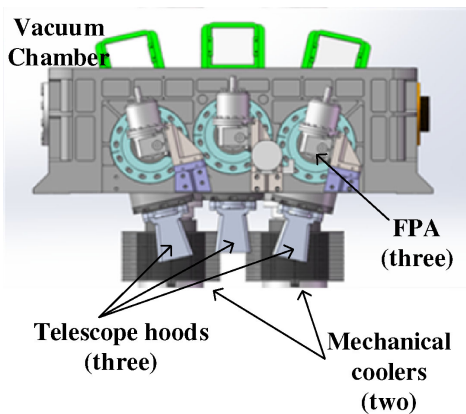
the structure of the spectrometer is designed as a reflective triplet (RT) spectrometer [13]. Three RT spectrometers of the same design are placed in a cold box with a low temperature of 100 K [13]. The weight of ATHIS is approximately 35 kg, Fig. 1 shows the composition of ATHIS. Two high-power Stirling refrigerators are used to achieve the goal of low-temperature refrigeration. The three telescopes are of independent structure, which are placed outside the cold box and are separately connected with their spectrometer components inside the cold box. The fronts of the three small telescopes are equipped with separate optical shields. Figs. 2 and 3 shows the structure and raytrace of the RT spectrometer in a single module, respectively. To ensure the operation of ATHIS under different conditions, the electronic control cabinet is also designed for power supply and detector signal acquisition. During flight, ATHIS is installed on a specific gyro-stabilized platform (Leica Geosystems PAV80) to control the line of sight. An independent high-precision IMU (PosPac 610 Applanix) is rigidly connected to the platform, which can be used for geo-referencing of the collected data.
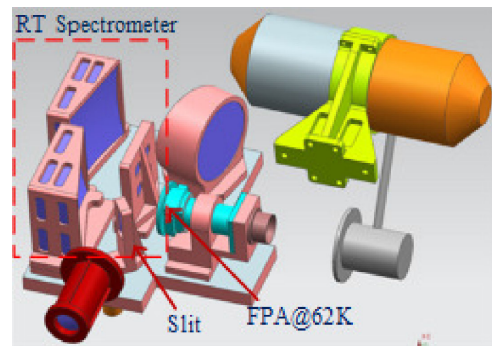
C. Detection-Sensitivity Optimization Method

Detection sensitivity is the most important technical metric of a TIR hyperspectral imager. ATHIS adopts the HgCdTe infrared focal plane, and its dark current level is on the order of 10^{-11} A. Although a 100 K spectrometer has been designed, the existence of dark current is still the main factor limiting the exposure time to continue to increase. For the purpose of good detection sensitivity under an exposure time as long as possible (6 ms), three optimization methods were used in the system design.

First, the slit was designed to be 45 μm. In theory, when the magnification of the spectrometer is 1 and the pixel size of the detector is 30 μm, the slit design is approximately 30 μm. The width of the slit directly limits the energy that can enter the system. If the slit is widened to 45 μm, the target energy entering the system can be greatly increased, but the consequence is the reduction of spectral resolution. Meng *et al*. [14] analyzed the relationship of slit width, spectral sampling interval, and spectral resolution in detail and verified by experiments. The results show that the spectral resolution does not decrease linearly with the increase of slit width. That is to say, when the slit is increased to 1.5 times the pixel size, the spectral resolution is not directly
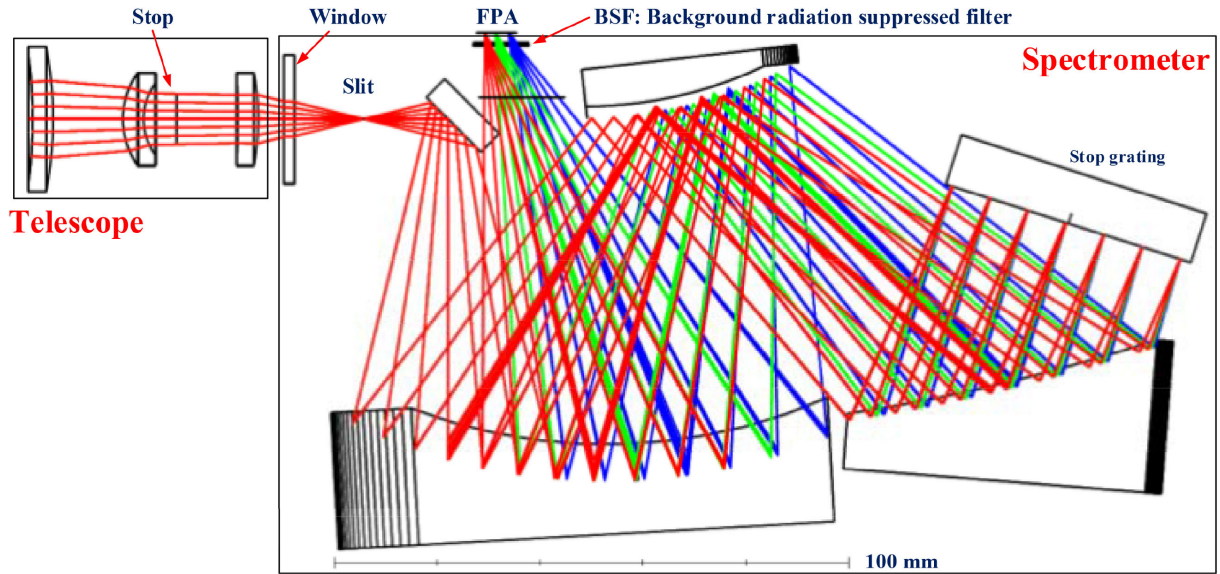
Fig. 3.   Raytrace of a single module.

reduced by 1.5 times, but it will be slightly better. Actually, after testing, the spectrum resolution of ATHIS can still reach 40 nm, and the direct benefit is that the incident energy is increased 1.5 times.

The second optimization method is choosing a smaller relative aperture (F#). Under the premise of a certain pixel size, the target energy received by the system is inversely proportional to the aperture factor. The aperture factor of ATHIS is designed as 2, which is much faster than that of the conventional short-wave infrared hyperspectral instruments, and can effectively increase the energy that the system can receive.

The last method of improving the sensitivity of the system is to accumulate and average the signals many times [15]. This method is one of the common methods of improving the detection sensitivity of an infrared imaging system. The precondition of realizing the scheme is that the instrument can sample multiple times in the dwell time of the same pixel position during remote-sensing imaging. In low-altitude remote sensing, the aircraft's flight speed is approximately 200 km/h, and the designed spatial resolution of ATHIS is 2 m@2000 m. At this time, ATHIS has more than 6 times of accumulation capability, which can improve the detection sensitivity by approximately 2.5 times.

III. VALIDATION EXPERIMENTS

To validate the performance of ATHIS in terms of emissivity-spectrum inversion, combined with the instrument and the feasibility of experiments, a laboratory mineral emissivity measurement experiment and a small-scale aerial remote-sensing experiment were carried out and the results reported herein.

A. Laboratory Measurement Experiment

The background environment of the laboratory is quite different from that of the outdoor atmosphere. The laboratory background consists of relatively stable artificial targets with high emissivity, such as walls and ceilings, whereas the outdoor clear atmosphere background has low emissivity. Therefore, in laboratory measurement experiments, when the background temperature is close to the sample temperature, it is easy to form a "pseudoblackbody" phenomenon [16]. To avoid this phenomenon, the experimental steps taken in the laboratory are the following.

1) Instrument Preheating and Configuration: First, turn ON the power supply of the TIR hyperspectral imager, and the refrigeration part of the device starts to work. After the temperature of the instrument's low-temperature system is stabilized to 100 K, open the data-acquisition software and configure the frame rate, frame number, storage path, filename, and other parameters.

2) Instrument Radiometric Calibration: Ces200-06 low-temperature blackbody was used to calibrate the TIR hyperspectral imager. The size of the blackbody radiation surface is 20 cm^2, the uniformity index is better than ± 0.05 °C(@23 °C), the temperature accuracy is $\pm$scura (full range), and the stability is $\pm 0.05\%$ within 30 min.

3) Sample Measurement: To increase the temperature difference between the sample and the laboratory background as much as possible, the sample minerals were placed on a heating plate and heated to approximately 50 °C. After warming, the sample was put into the FOV of the instrument to collect data, and the temperature of sample before and after data collection was also measured using a contact thermometer. The experimental setup is shown in Fig. 4.

4) Background Radiation Measurement: After the data collection of each sample, the background radiation was measured by means of recording the reflected radiation from a prepared gold panel that was placed onto the same position as the sample and can fill the FOV of the instrument. The gold panel is a gold-coated diffuse reflector with a reflectance of 0.94 in the TIR spectrum. After data collection, the physical temperature of the gold panel was measured and recorded with the same thermometer.
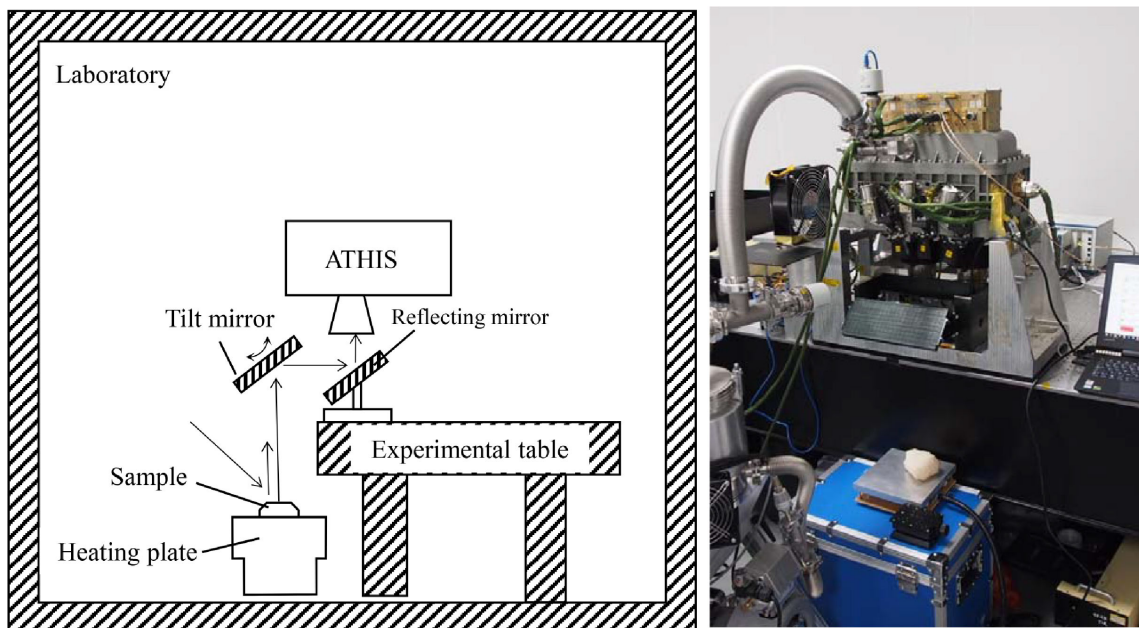
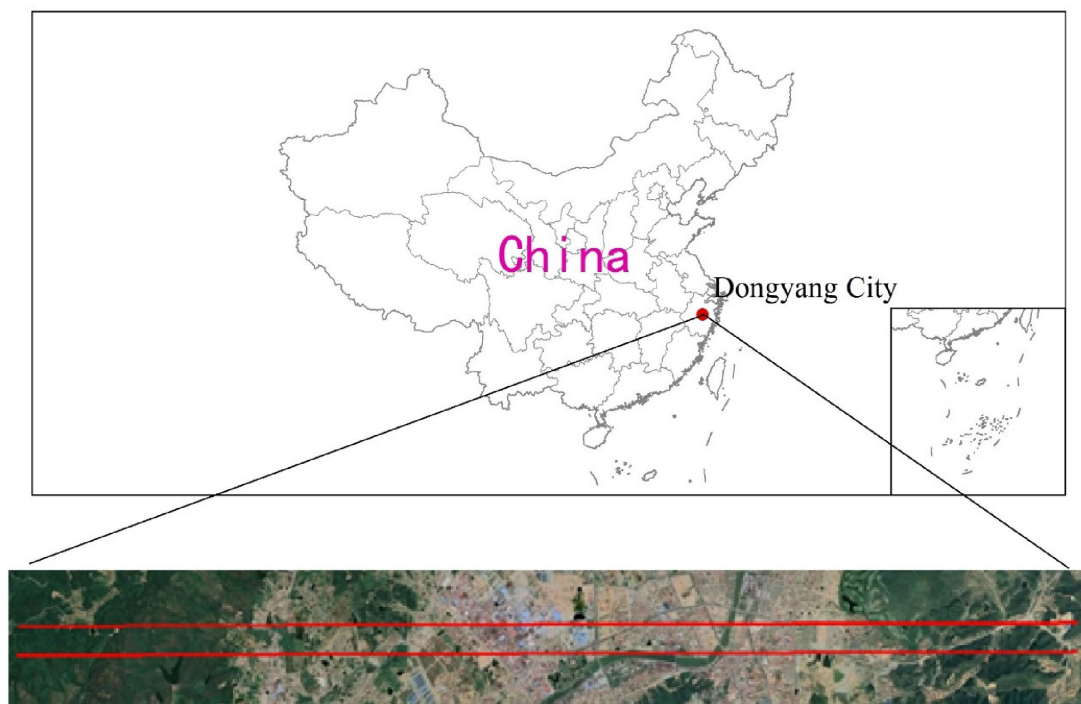Fig. 4. Setup of laboratory measurement experiment.

Fig. 5. Schematic map of the flight lines.

B. Aerial Remote-Sensing Experiment

With the aim of verifying the ability of ATHIS to obtain remote-sensing data in a larger range, an aerial remote-sensing experiment was carried out in Hengdian Town, Dongyang City, Zhejiang Province, China (120°18′11″E, 29°09′20″N) on May 24, 2019. The schematic map of the flight lines is shown in Fig. 5.

The height above ground level of the flight was 2000 m and the corresponding spatial resolution was 2 m. At the same time, ground emissivity and temperature measurement experiments were carried out simultaneously, and the polytetrafluoroethylene target was rolled out, as shown in Fig. 6. During the experiment, the weather was sunny and breezy, and the temperature was approximately 26.6 °C.
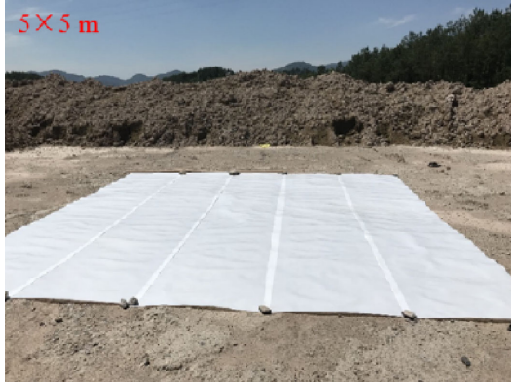
5×5 m

Fig. 6. Polytetrafluoroethylene target.

IV. DATA PROCESSING

A. Laboratory Measurement Experiment

The processing of laboratory data is mainly done to obtain the spectral emissivity of samples. As shown in Fig. 7, the bad pixels in the original TIR hyperspectral data are first corrected according to the bad pixel mask. Then, radiometric calibration is carried out according to the blackbody data of the laboratory. Next, the background radiation in the laboratory is calculated according to the data of the gold panel. Finally, the spectral emissivity of the sample is calculated from the sample radiance by combining the background radiance and the measured sample temperature.

1) Repair of Bad Pixels: The response of the bad pixels is abnormal and the pixel values are not available. Usually, the instrument extracts the bad pixels from the blackbody images of different temperatures measured in the laboratory to form the bad-pixel mask. In the data processing, the bad pixels are corrected according to the mask. In bad-pixel repair, for each frame of TIR hyperspectral data, the mean value of nonbad pixels in the 3×3 neighborhood of each bad pixel is searched according to the mask as the corrected value of the bad pixel, and the repair of all frames is completed one by one. If there are no nonbad pixels in the 3×3 neighborhood, the search window will be expanded until the average value of nonbad pixels can be obtained. Fig. 8 shows a frame of a 40 °C blackbody data cube before and after repair, and it can be seen that the bad pixels have been well corrected.

2) Radiometric Calibration: In radiometric calibration, the traditional hyperspectral data relative radiometric calibration and absolute radiometric calibration are combined into one process, and the digital number (DN) value is directly converted into radiance data. The calculation formula is

$$L_{\text{lab}}(i, j, k) = a_{\text{lab}}(i, k) \times \text{DN}_{\text{lab}}(i, j, k) + b_{\text{lab}}(i, k) \quad (1)$$

where i, j, and k are the ordinal numbers of the sample, line, and band of the TIR hyperspectral data, respectively; $L_{\text{lab}}(i, j, k)$ is the radiance of the measured sample or gold panel; $\text{DN}_{\text{lab}}(i, j, k)$ is the DN of raw data; and $a_{\text{lab}}(i, k)$ and $b_{\text{lab}}(i, k)$ are the radiometric calibration coefficients, which can be calculated from the blackbody imaging data of different temperatures. Fig. 9 shows an example of radiometric calibration. There is

still some columnwise residual noise remaining. The reason for the residual noise is that the pixel response in the scan line has fluctuated during the data collection, so the radiation calibration coefficient calculated with the blackbody calibration data cannot completely eliminate the nonuniformity.

3) Calculation of Background Radiance: The radiative transfer equation of the gold panel measurement process can be expressed as

$$L_{\text{lab,panel}}(\lambda) = B(T_{\text{panel,s}}, \lambda)\varepsilon_{\text{panel}}(\lambda)$$
$$+ \left[1 - \varepsilon_{\text{panel}}(\lambda)\right] L_{\text{lab},d}(\lambda) \quad (2)$$

where $L_{\text{lab,panel}}(\lambda)$ is the at-sensor radiance, λ the wavelength, and $T_{\text{panel,s}}$ is the surface temperature of the gold panel. $B(T_{\text{panel,s}}, \lambda)$, calculated from Planck's law, is the radiance corresponding to the blackbody with temperature of $T_{\text{panel,s}}$, $\varepsilon_{\text{panel}}(\lambda)$ is the emissivity of the gold panel, and $L_{\text{lab,d}}(\lambda)$ is background radiance of the laboratory. The background radiation of the laboratory can be calculated by measuring the reflected radiation and temperature of the gold panel, and the calculation formula is

$$L_{\downarrow}(\lambda) = \left[L_{\text{panel}} - \varepsilon_{\text{panel}}B(T_{\text{panel}})\right] / \left(1 - \varepsilon_{\text{panel}}\right). \quad (3)$$

In laboratory measurements, a gold panel supplied by Labsphere, Inc., was utilized, and the emissivity ($\varepsilon_{\text{panel}}$) is 0.06. Fig. 10 shows one calculated background radiance measured in laboratory. Compared with the spectrum of the atmospheric radiation in the clear sky, the spectral characteristics of the variance in spectral radiance features in the laboratory are much less.

4) Calculation of Sample Emissivity: Remote sensing in the laboratory is different from remote sensing in the field in that there is no so-called "burr" in the infrared background radiation under laboratory conditions. In the process of laboratory measurement, the sample is relatively close to the instrument (approximately 0.5 m). According to relevant research, when the target distance is less than 1 m, the atmospheric absorption and radiation can be ignored [17], [18]. Thus, the transfer equation of TIR radiation in the laboratory is simplified as

$$L_{\text{lab,sample}}(\lambda) = B(T_{\text{sample}}, \lambda)\varepsilon_{\text{sample}}(\lambda)$$
$$+ \left[1 - \varepsilon_{\text{sample}}(\lambda)\right] L_{\text{lab,d}}(\lambda) \quad (4)$$

where $L_{\text{lab,sample}}(\lambda)$ is the radiance of sample, T_{sample} is the temperature of the sample, $B(T_{\text{sample}}, \lambda)$ is the sample's radiance corresponding to the blackbody with a temperature of T_{sample}, and $\varepsilon_{\text{sample}}(\lambda)$ is the emissivity of the sample at wavelength λ. Together with the measured at-sensor radiance and temperature of the sample and the calculated background radiance using (3), the calculation formula of sample emissivity can then be expressed as

$$\varepsilon_{\text{sample}}(\lambda) = \left[L_{\text{lab,sample}}(\lambda) - L_{\text{lab,d}}(\lambda)\right] /$$
$$\times \left[B(T_{\text{sample}}, \lambda) - L_{\text{lab,d}}(\lambda)\right]. \quad (5)$$

B. Airborne Data Processing

The aim of airborne TIR hyperspectral data processing is to obtain the temperature and emissivity of ground objects from
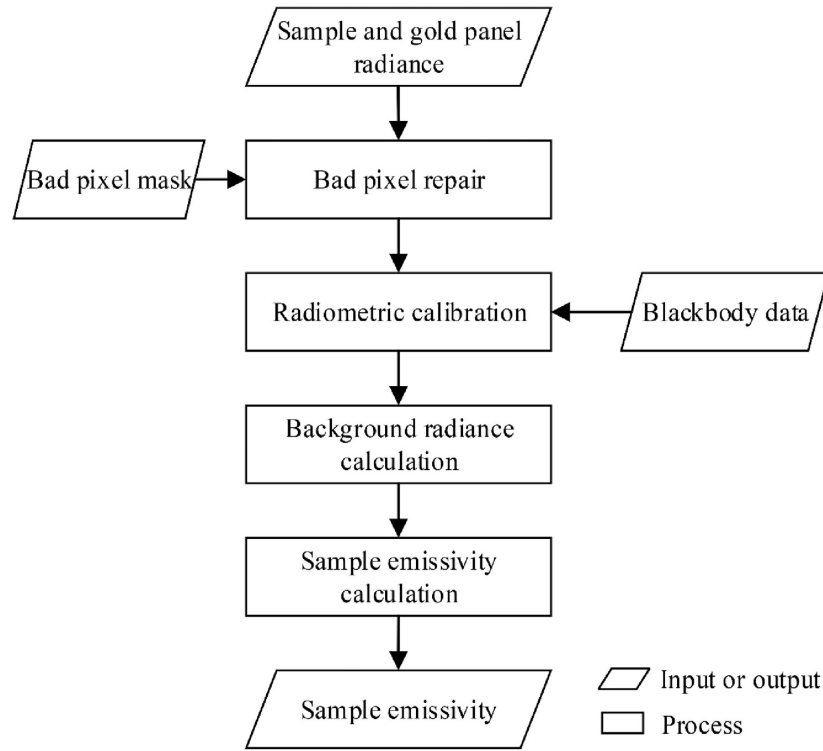
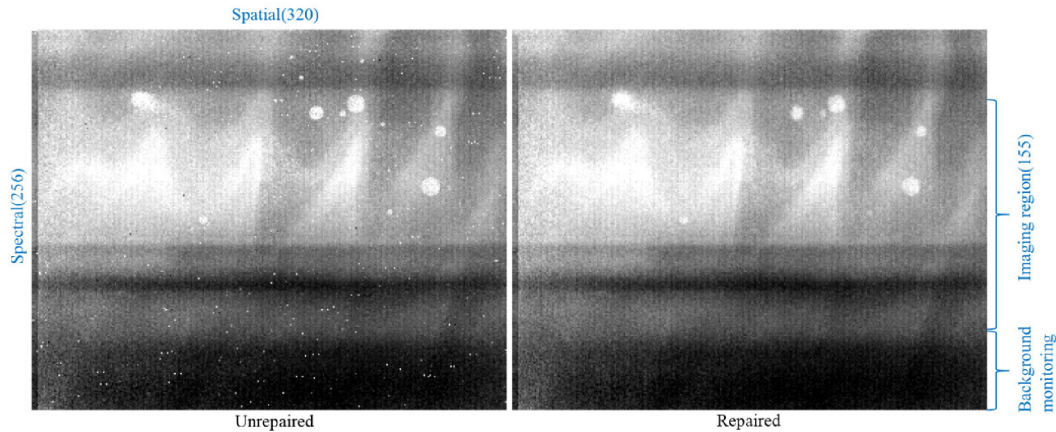Fig. 7. Flowchart of laboratory data processing.

Fig. 8. Single frame of 40 °C blackbody data cube measured in laboratory before and after repair.

the raw data; that is, to convert the DN value of the raw data into temperature and emissivity. As shown in Fig. 11, the bad pixels in the original TIR hyperspectral data are first corrected according to the bad-pixel mask. Then, according to the on-board blackbody data recorded during flight, radiometric calibration is carried out, and the DN value converted into the radiance. Next, scene-based nonuniformity correction is carried out to eliminate the residual stripe noise of radiometric calibration. Based on the aforementioned process, the difference between the reference target radiance in the image and the simulated radiance of the reference target is compared to determine whether field calibration is needed. If there is no need for field calibration, the atmospheric correction of TIR hyperspectral data will be directly executed to obtain the ground-leaving radiance. Finally,

combined with the simulated downward atmospheric radiance, the temperature and emissivity are retrieved from the ground-leaving-radiance images.

1) Repair of Bad Pixels: Similar to the laboratory data, the repair of bad pixels of airborne data is also based on the sequence of imaging frames in which the mean value of nonbad pixels in the 3×3 neighborhood is selected as the value of bad pixels. Fig. 12 shows a frame of 40 °C blackbody data cube before and after repair.

2) Radiometric Calibration: Similar to the radiometric calibration of laboratory data, the calculation formula for radiometric validation of airborne data is

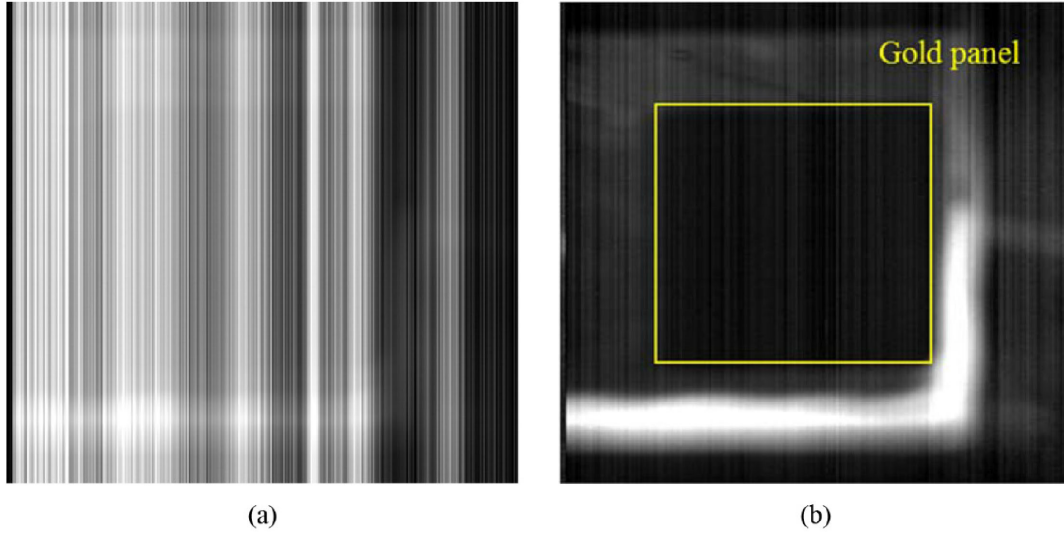$$L(i, j, k) = a(i, k) \times DN(i, j, k) + b(i, k) \tag{6}$$

Fig. 9. 110th band image of gold panel data cube measured in laboratory before and after radiometric calibration. (a) Uncalibrated. (b) Calibrated.
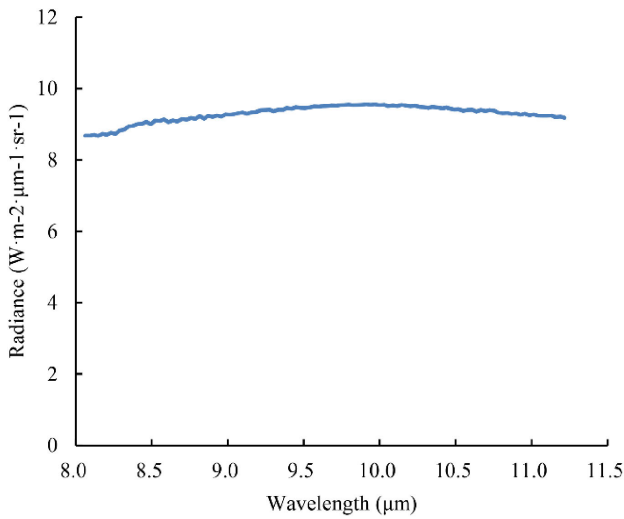

Fig. 10. Calculated background radiance measured in laboratory.

where $L(i, j, k)$ is the converted radiance, $\mathrm{DN}(i, j, k)$ is the DN of raw data, and $a(i, k)$ and $b(i, k)$ are the radiometric calibration coefficients, which can be calculated from the on-board blackbody data. Fig. 13(a) and (b) shows the images of airborne data cube before and after radiometric calibrated.

3) Nonuniformity Correction: After bad-pixel restoration and radiometric calibration, most of the systematic noise caused by the instrument can be removed. However, some residual stripe noise still exists in their column direction. This originates from the pixel response in the scan line that has fluctuated during the data collection. In this article, the method of moment matching is used to correct the nonuniformity of the calibrated TIR hyperspectral data. The correction is carried out in a column-by-column manner, and the calculated formula is

$$\hat{L}(i, j, k) = \frac{\sigma_{i,k}}{\sigma_k} L(i, j, k) + \mu_k - \frac{\sigma_{i,k}}{\sigma_k} \mu_{i,k} \qquad (7)$$

where $\hat{L}(i, j, k)$ is the corrected radiance of pixel (i, j, k), $L(i, j, k)$ is the uncorrected pixel value corresponding to $\hat{L}(i, j, k)$, $\mu_{i,k}$ and μ_k are the mean values of sample and the reference mean value of the full image of band k, respectively, and $\sigma_{i,k}$ and σ_k are the standard deviations corresponding to $\mu_{i,k}$ and μ_k, respectively. Fig. 13(c) shows the image of airborne data cube after calibration and nonuniformity correction, and the residual stripe noise after radiometric calibration is eliminated.

4) Simulation of Atmospheric Radiative Transfer: In the TIR region, assuming that the atmosphere is in a state of local thermal equilibrium, and neglecting the effects of scattering, the equation of atmospheric radiative transfer can be expressed as [19]

$$L(\lambda) = B(T_s, \lambda)\varepsilon(\lambda)t(\lambda) + [1 - \varepsilon(\lambda)] L_d(\lambda)t(\lambda) + L_p(\lambda) \qquad (8)$$

where λ is the wavelength, $L(\lambda)$ is the at-sensor radiance, T_s is the temperature of the ground object, $B(T_s, \lambda)$ is the sample's radiance corresponding to the blackbody with a temperature of T_s, $\varepsilon(\lambda)$ is the emissivity, $t(\lambda)$ is the atmospheric transmittance, $L_d(\lambda)$ is the downward atmospheric radiance, and $L_p(\lambda)$ is the path radiance of the atmosphere. Indeed, $t(\lambda)$, $L_d(\lambda)$, and $L_p(\lambda)$ in the radiative transfer equation are primarily affected by the atmospheric conditions, and they summarize the role of the atmosphere in the transfer of TIR radiation from ground objects to sensors. In this article, we simply call them radiative transfer parameters. Atmospheric radiative transfer simulation is mainly done to input meteorological data (such as atmospheric temperature and humidity profile), sensor observation geometry, and other parameters into the atmospheric radiative transfer software MODTRAN [20] to obtain the radiative transfer parameters $t(\lambda)$, $L_d(\lambda)$, and $L_p(\lambda)$. The meteorological data used in this article are the National Center for Environmental Prediction meteorological data [21] used in the aerial remote-sensing experiment.

5) Field Calibration: Because the sensor is in a complex environment in the process of data acquisition, coupled with the aging of components, sometimes the on-board calibration
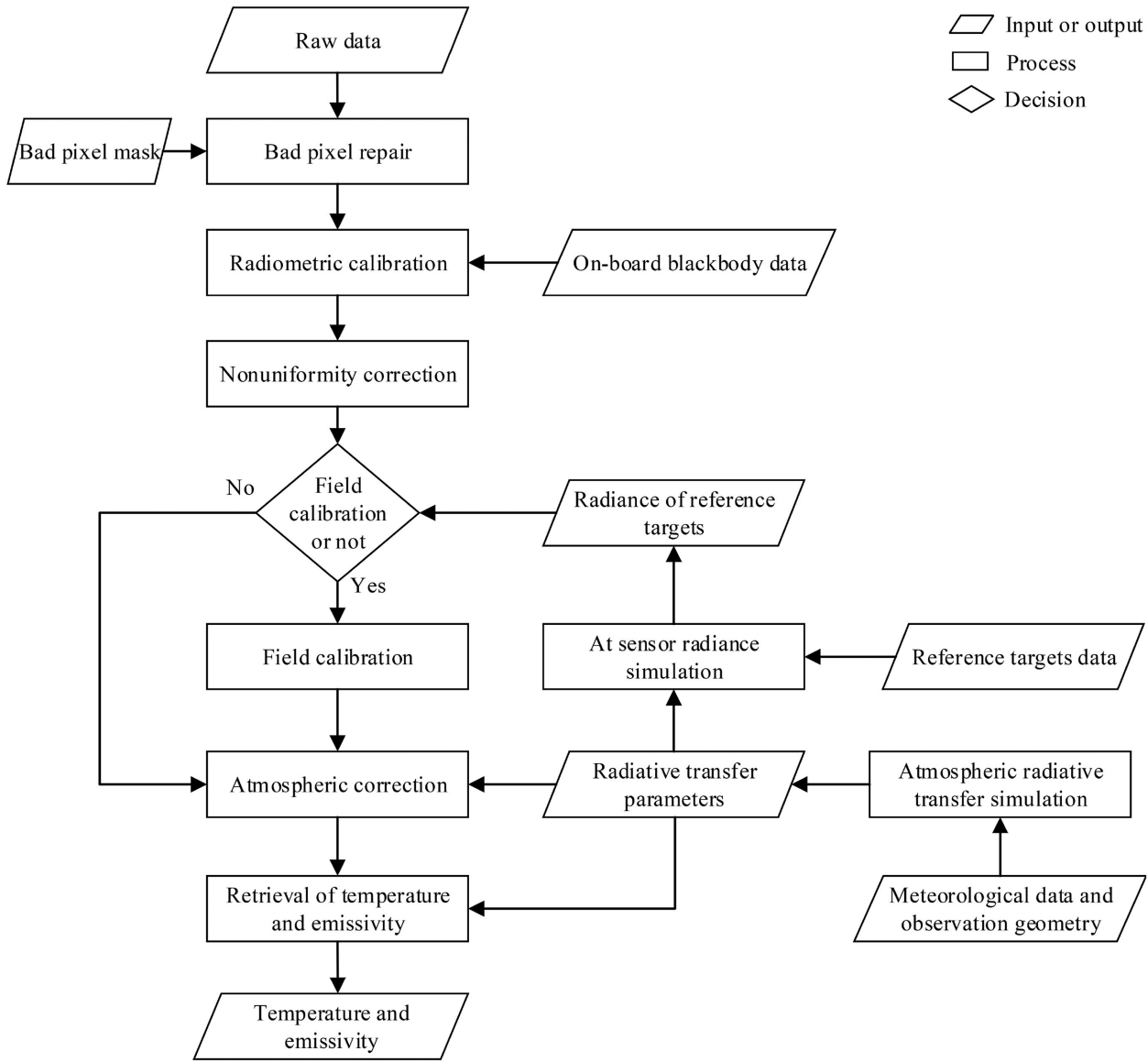
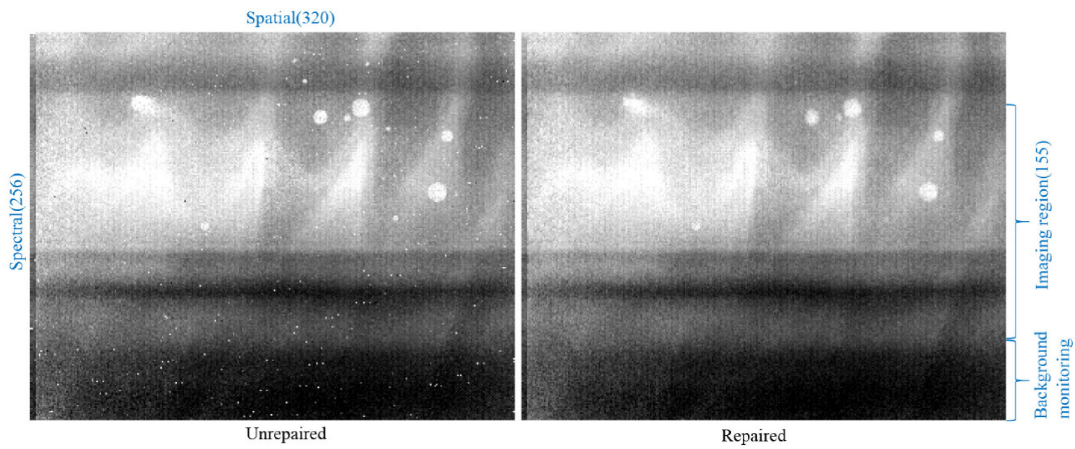Fig. 11.   Flowchart of airborne data processing.

Fig. 12.   Single frame of 23.0 °C on-board blackbody data cube before and after repair.
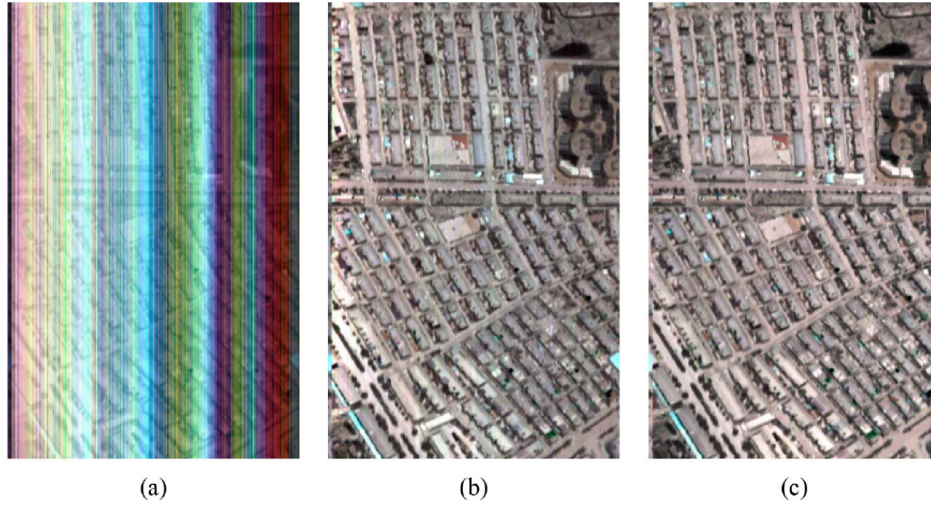
Fig. 13.   Images of airborne data cube before and after calibration and nonuniformity (R:10.644 μm, G:9.485 μm, and B:8.906 μm). (a) Uncalibrated. (b) Calibrated. (c) Nonuniformity corrected.
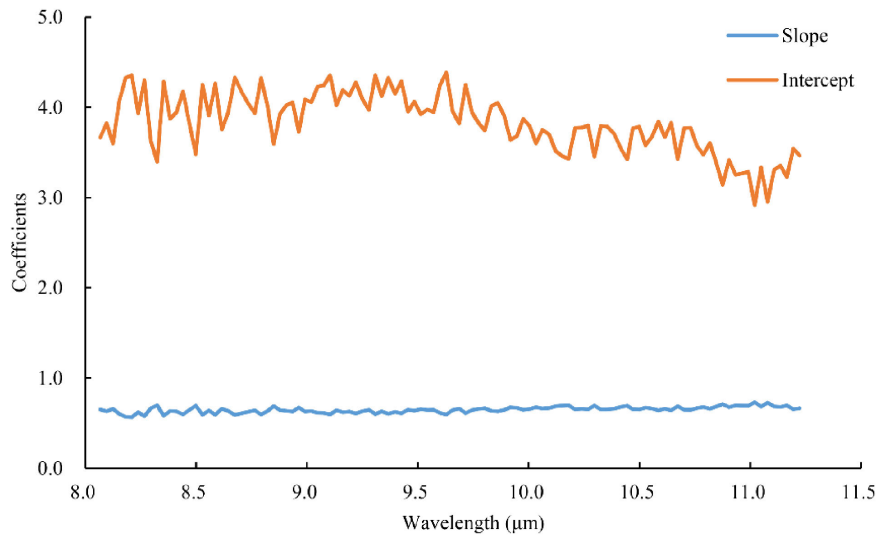

Fig. 14.   Calculated field calibration coefficients.

blackbody of an instrument may incur an inaccurate temperature measurement, which directly leads to the systematic deviation of radiometric calibration on basis of on-board blackbody data. At this time, field calibration usually is used as a vicarious calibration. Generally, field calibration is that done in the flight experiment, and the ground reference targets and atmospheric condition measurements are carried out synchronously. Based on the ground synchronous measurements, the at-sensor radiances of the targets are simulated and obtained, and the relationship between the simulated radiance and target radiance in the radiometric calibrated image can be established so as to achieve recalibration. The calculation formula is

$$L'(i, j, k) = a'(k) \times \hat{L}(i, j, k) + b'(k) \qquad (9)$$

where $L'(i, j, k)$ is the recalibrated radiance through field calibration; $a'(k)$ and $b'(k)$ are the coefficients of field calibration,

which can be calculated from the simulated radiance and target radiance in the radiometric calibrated image using the least-squares method. The selection of reference target is one of the important factors that affects the accuracy of field calibration. For the TIR region, the emissive spectrum properties of a water body are similar to the blackbody and the emissivity is stable, and its temperature is easy to measure, so the water body was selected as the reference target. Fig. 14 shows the calculated coefficients of field calibration.

6) Atmospheric Correction: It can be seen from the atmospheric radiative transfer equation in the TIR region that the first two parts on the right-hand side of the equation are mainly related to the characteristics of the ground objects, which can be called the ground-leaving radiance, and the third part is only related to atmospheric conditions. It is noted that $L_g(\lambda_i)$ is the ground-leaving radiance, and then the at-sensor radiance can be
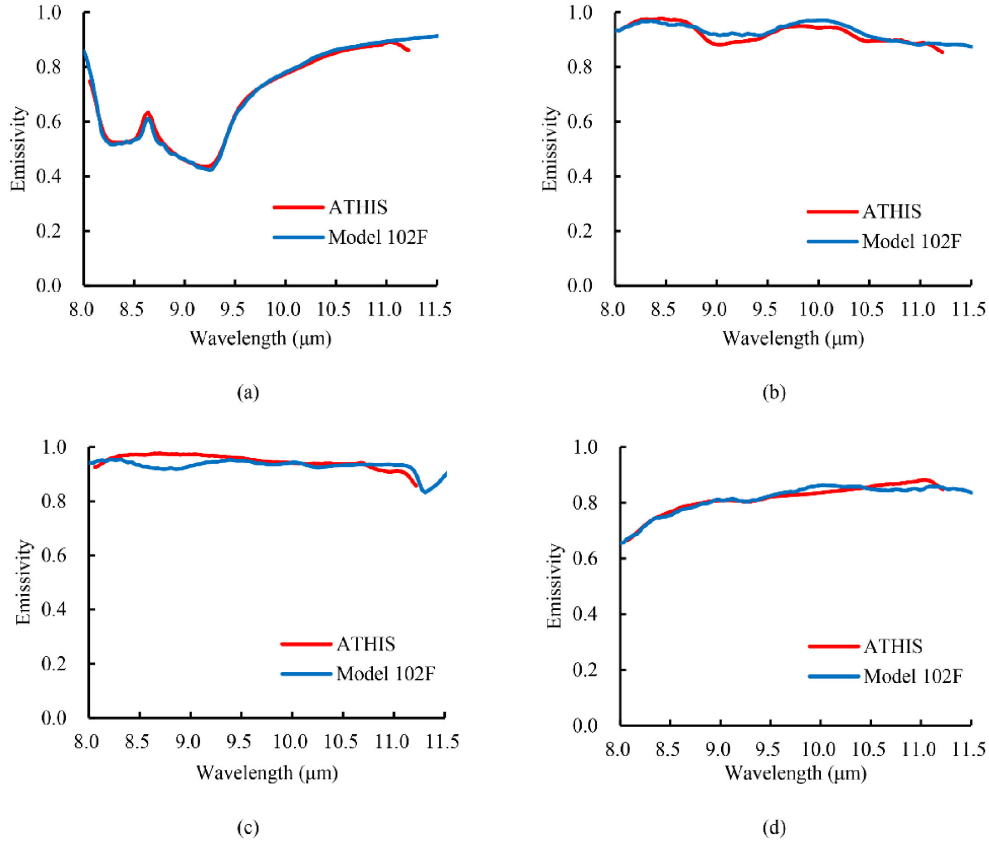
Fig. 15. Emissivity spectra of mineral samples measured by ATHIS in laboratory. (a) Quartz. (b) Epidote. (c) Calcite. (d) Fluorite.

expressed as

$$L(\lambda) = L_g(\lambda)t(\lambda) + L_p(\lambda) \tag{10}$$

and $L_g(\lambda_i)$ is expressed as

$$L_g(\lambda) = B(T_s, \lambda)\varepsilon(\lambda) + [1 - \varepsilon(\lambda)] L_d(\lambda). \tag{11}$$

It can be considered that the atmospheric correction is carried out to obtain accurate atmospheric transmittance, atmospheric downward radiance, and atmospheric path radiance, to obtain the ground-leaving radiance in (9), from which the temperature and emissivity of the ground object are retrieved.

At present, there are two kinds of atmospheric correction methods that can be used for TIR hyperspectral data. The first is to use the retrieved or measured atmospheric profiles, supplemented by the mature atmospheric radiative transfer model. However, it is not easy to obtain the pixel-scale atmospheric profile, and it is also difficult to obtain it synchronously with the TIR hyperspectral data. The second atmospheric correction method is based on the spatial and spectral information of the TIR hyperspectral data, directly from the TIR hyperspectral remote-sensing data itself to calculate the atmospheric parameters, such as atmospheric transmittance, atmospheric downward, and path radiance. The second kind of method mainly includes the autonomy atmospheric compensation method [22] and the in-scene atmospheric compensation method [23]. These methods can be thought of as scene-based atmospheric correction methods, which more or less have some requirements for the

scene. The main purpose of this article is to test the performance of ATHIS, especially its performance in retrieving the emissivity spectrum of the ground object. Therefore, the first method is selected for atmospheric correction.

7) Temperature and Emissivity Separation: Temperature and emissivity are in a coupling state in the expression of the ground-leaving radiance shown in (10). In the equation system composed of (9) of a different band, the unknown number is always equal to the equation number plus 1. Therefore, some strategies must be undertaken to make the equations solvable and to achieve the separation of temperature and emissivity. The iterative perspective smooth method proposed in [19] and [23], which is one of the most widely used methods. It is based on the assumption that the spectral curve of the atmospheric downward radiation is not smooth in high spectral resolution, and the spectral emissivity spectrum of the ground object is relatively smooth. By estimating and continuously optimizing the temperature, the obtained spectral emissivity of the ground object is the smoothest. The criterion for measuring spectral smoothness is

$$S = \sum_{k=2}^{N_k-1} [\varepsilon_k - (\varepsilon_{k-1} + \varepsilon_k + \varepsilon_{k+1})/3] \tag{12}$$

where S is the spectral smoothness, N_k is the band number, and ε_k is the emissivity of band k. The process of optimizing the
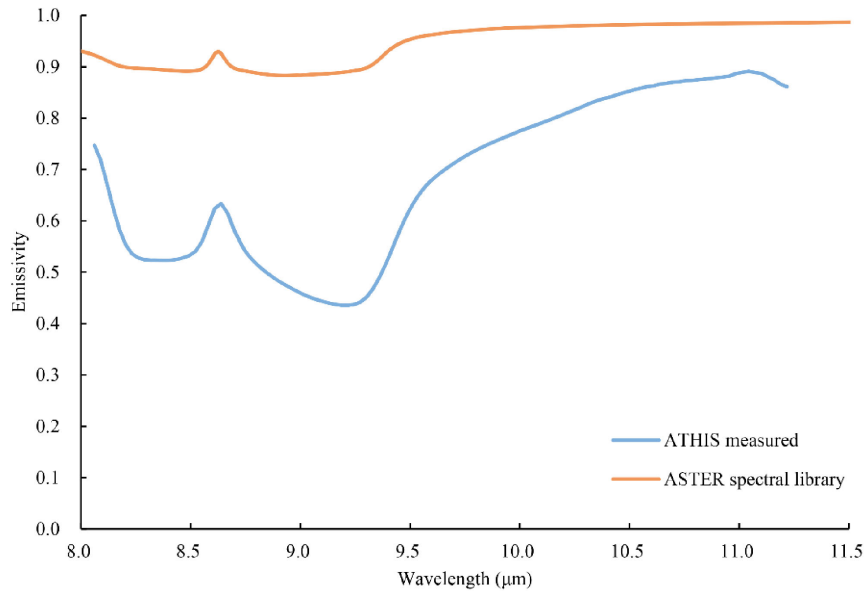
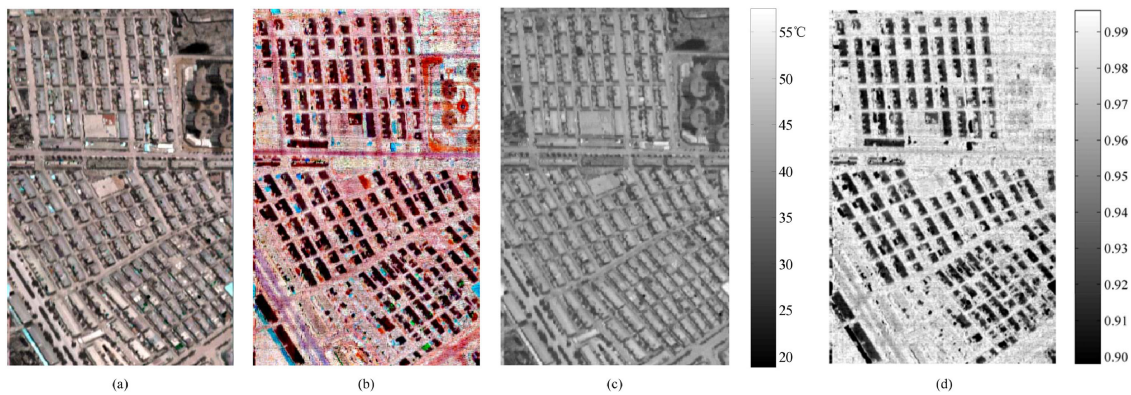Fig. 16.   Emissivity spectrum of quartz in ASTER spectral library.

Fig. 17.   Images of radiance, emissivity, and temperature in building area. (a) False color radiance image (R:10.644 μm, G:9.485 μm, and B:8.906 μm). (b) False color emissivity image (R:10.644 μm, G:9.485 μm, and B:8.906 μm). (c) Temperature image. (d) Grayscale emissivity image (10.644 μm).
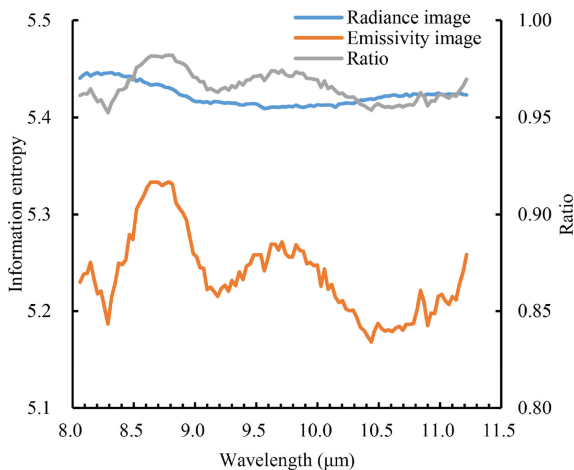

Fig. 18.   Image definition statistics of emissivity and radiance in building area. Blue and orange curves correspond to the left y-axis, and the gray curve corresponds to the right y-axis.

temperature is to minimize the smoothness s, that is

$$dS(T_s)/dT_s \cong 0. \tag{13}$$

After the temperature of the ground object is determined, the emissivity of each band can be calculated from the corresponding expression of the ground-leaving radiance.

V. Results and Analysis

A. Mineral Identification Potential

Using the technical process described in Section IV-A, the TIR hyperspectral data of minerals measured in the laboratory were processed, and the emissivity spectrum of mineral samples finally obtained, as shown in Fig. 15. Quartz, epidote, calcite, and fluorite were selected as the measured samples in the laboratory. The designed spectral response range of the ATHIS is 8–12.5 μm. Because of the low sensitivity of 11.2–12.5 μm, which leads to the current effective detection spectrum range
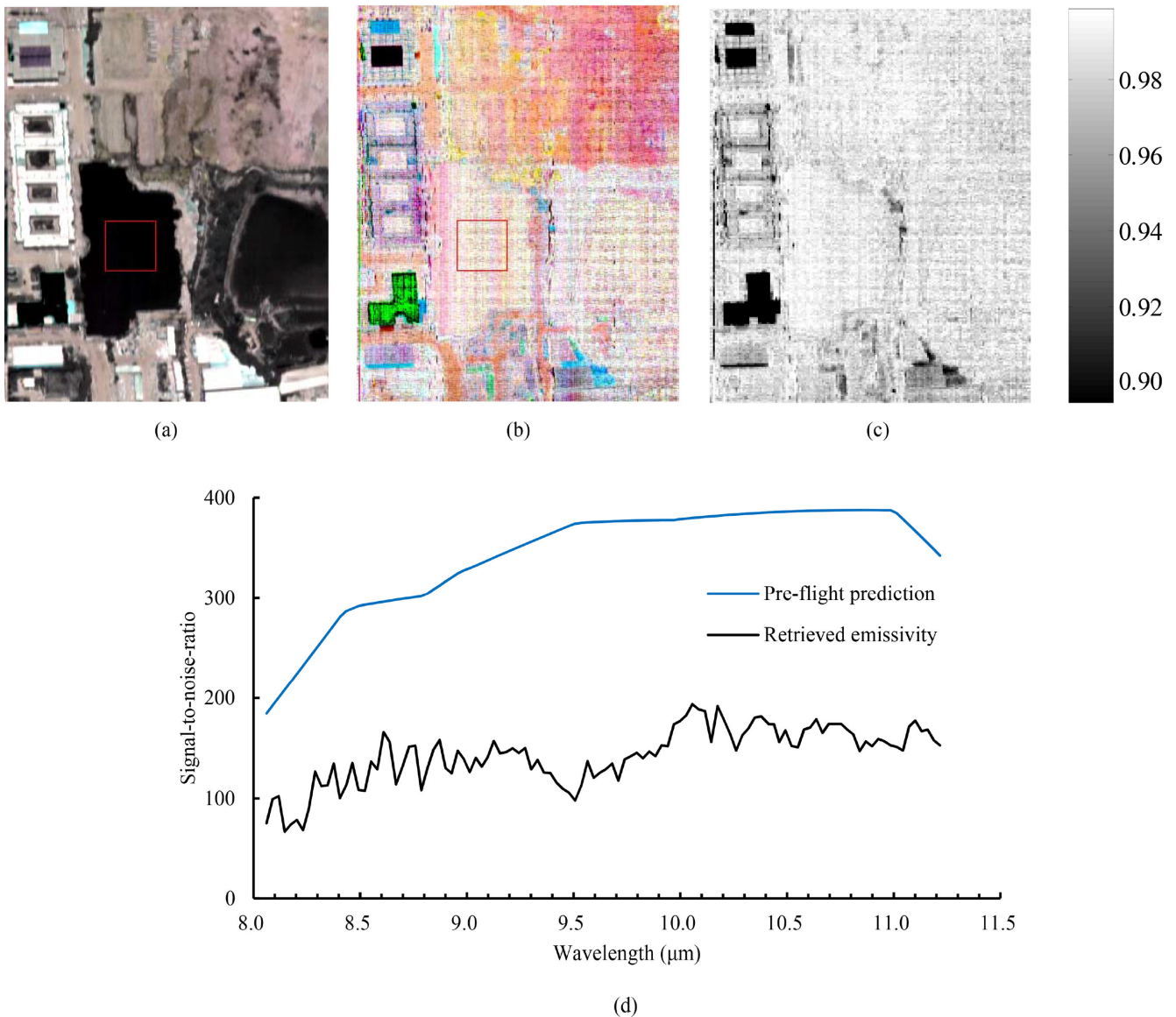
Fig. 19. SNRs of emissivity of uniform water and preflight prediction. (a) False color radiance image. (b) False color emissivity image. (c) Grayscale emissivity image (10.644 μm). (d) SNR. Black curve corresponds to SNR of red box in (b). Blue curve is SNR of preflight prediction using ATHIS specifications in a sensor performance model with 25 °C blackbody as radiation source.

being 8–11.2 μm, this article mainly shows the data processing results of 8–11.2 μm. According to the variation trend of the spectra and the positions of peaks, the emissivity spectra measured by ATHIS were basically the same as that measured by the model 102F FTIR spectrometer, except for some small differences in some wavelengths. It was calculated that the cosine values of the spectral angle between the four emissivity spectra measured by ATHIS and the model 102F spectrometer were 0.9999, 0.9999, 0.9997, and 0.9998. In particular, the quartz spectral curve in Fig. 15(a), except for the slight difference in curvature near individual inflexion and extreme points due to the different spectral resolutions, the positions of the peaks and valleys of the emissivity spectral curve measured by ATHIS and the model 102F spectrometer completely coincided (such as the emission peak near 8.638 μm). Compared with the peak

value (8.626 μm) of the quartz emissivity spectrum in the ASTER spectral library shown in Fig. 16, the mismatch degree of maximum position was only 0.012 μm, which can be considered as the error caused by the convolution effect of spectral resolution difference between devices. The discrepancy was in the (8–9)-μm wavelength range, and the emissivity measured by ATHIS was smaller than that of ASTER. However, the emissivity values measured and reported in this article were very close to the results measured by HyperCam [24]. This may have been affected by the different shapes of the samples in the actual measurement and the spectral library. Through this test, we can basically conclude that ATHIS has the capacity to accurately measure the spectral emissivity of minerals, which can meet the needs of mineral recognition based on emissivity spectrum characteristics.
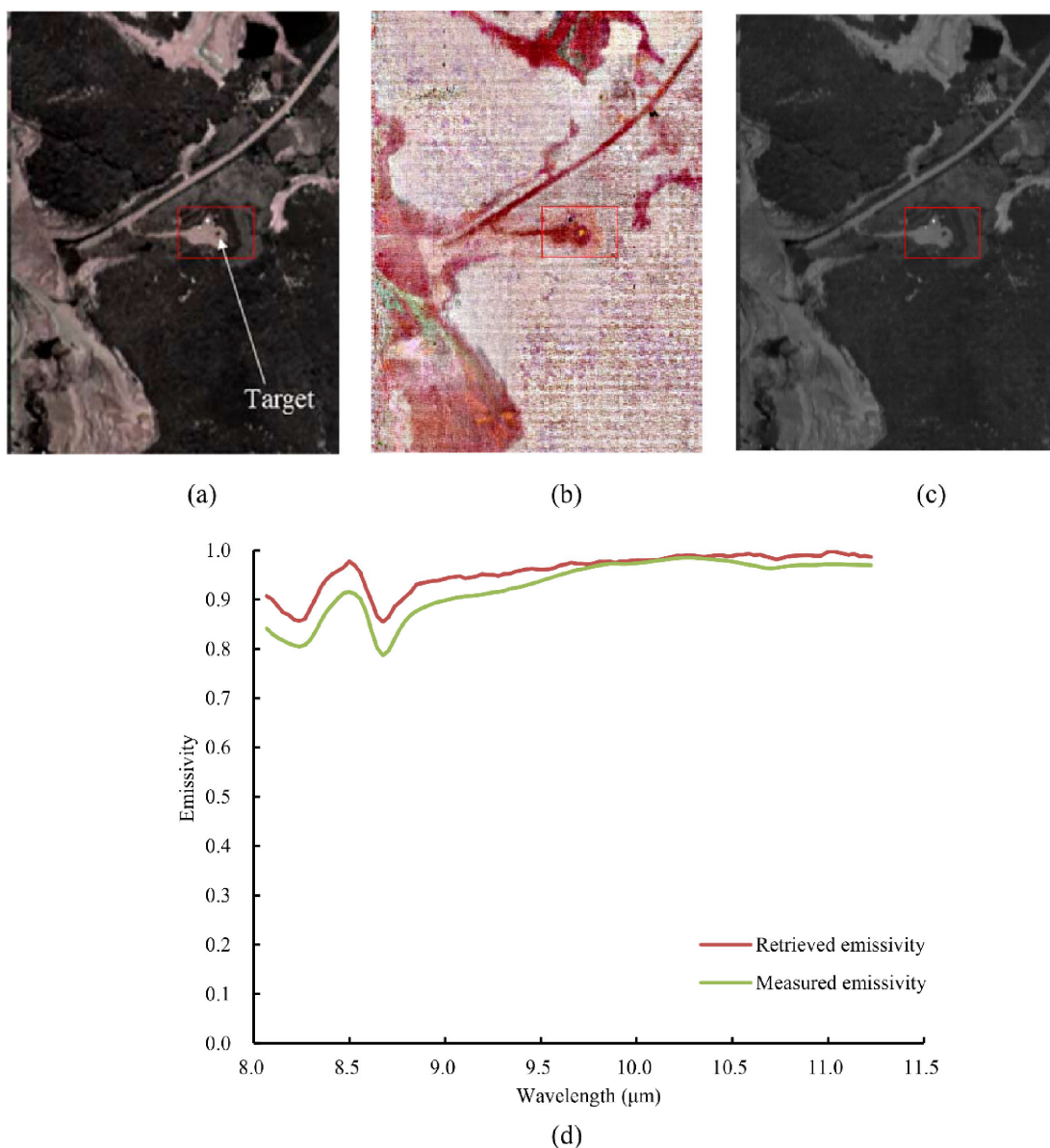
Fig. 20. Layout and validation of target. (a) Radiance image. (b) Emissivity image. (c) Temperature image. (d) Retrieved and measured emissivity spectra of the target in (a).

B. Retrieved Emissivity Imagery

Using the technical process described in Section IV-B, the airborne data were processed, and finally the emissivity and temperature images of the ground objects were obtained. Fig. 17 shows the retrieved emissivity and temperature images of the built-up area of Hengdian Town. The color of the image is clearly layered. Whether in the radiance image, or in the inverted emissivity and temperature images, the buildings, roads, and other ground objects show clear outlines and different colors determined by their physical properties.

The curve in Fig. 18 shows that the information entropy (IE) calculated from the emissivity image in Fig. 17 varies with the wavelength. It can be seen from Fig. 18 that after the temperature information is extracted from the radiance image, the IE of the emissivity image was lower than that of the radiance image, but the reduced quantity was not very large. The ratio of IE between the emissivity and radiance images was larger than 0.95 in all bands, which shows that the definition of the image was not significantly reduced. Fig. 19 shows the signal-to-noise-ratio (SNR) curve of the emissivity image of uniform water and the preflight prediction using ATHIS specifications in a sensor performance model with a 25 °C blackbody as the radiation source. It can be seen that the predicted SNR is twice that of the emissivity image of water. The main reasons for this phenomenon may be: first, the slight fluctuation of water surface makes the emissivity uneven, and second, the temperature information is extracted. In addition, a third reason may be that the performance of the instrument may be reduced due to the impact of the working environment during the flight. For the SNR curve

of the emissivity image of water, except for the SNRs of bands 1 and 3–8 being lower than 100 (the lowest is 67), the SNRs of the other bands were all above 100. Band 70 has the largest SNR, i.e., 194. From the perspective of SNR, the spatial characteristics of retrieved emissivity images can satisfy the requirements of basic remote-sensing data applications (such as ground object classification and identification).

C. Ground Synchronous Validation of Emissivity

To validate the emissivity retrieval performance of ATHIS, a 5×5-m^2 polytetrafluoroethylene target (which is a kind of polymer synthetic material with spectral absorption characteristics between 8.0 and 9.0 μm) was rolled out on open ground, as shown in Fig. 6. The spatial resolution of the airborne data is 2 m, so the target can cover more than four pixels, and at least one pure pixel can be ensured, which satisfies the demand of ground synchronous validation. Fig. 20(a)–(c) shows, respectively, the radiance image, emissivity image, and temperature image of the target and its adjacent area. From the images, it can be clearly seen that the radiation difference between the target and surrounding area was significant, and it can be obviously distinguished. When the aircraft was over the top of the target, the emissivity of the target was measured using the model 102F FTIR spectrometer. Fig. 20(d) shows the comparison between the retrieved target emissivity and measured emissivity. It can be seen from the comparison that although there is a certain gap between the two in the specific emissivity value (possibly caused by the difference in the FOV and observation angle), they have the same wavelength variation trend, especially the peaks and valleys at 8.0–9.0 μm, and the spectral angle cosine value of the two reaches up to 0.9997. From the target validation experiment, the spectral performance of the retrieved emissivity image can satisfy the requirements of some basic remote-sensing data applications.

VI. Conclusion

With the aim of validating the performance of ATHIS, based on the analysis of the radiative transfer model and data-processing methods of TIR hyperspectral imaging, laboratory measurement experiments and the aerial remote-sensing experiment were carried out. From the aspect of mineral emissivity measurements in the laboratory, whether the comparison is with the measurement results of mature commercial FTIR spectrometers or other TIR hyperspectral imagers, similar measurement results are obtained in this article. From the aspect of aerial remote-sensing experiments, the retrieved emissivity image is clear and the emissivity spectrum can accurately reflect the emission characteristics of the ground object. This fully proves that ATHIS can obtain accurate TIR hyperspectral remote sensing data, and the retrieved emissivity images from these data can meet the remote-sensing application requirements based on TIR hyperspectral images.

TIR hyperspectral remote sensing is deeply influenced by atmospheric absorption. In the process of temperature and emissivity retrieval, it is inevitable that accurate atmospheric information be obtained and the radiative transfer parameters be calculated. In this article, the problem is solved temporarily

by inputting the weather forecast data into the radiative transfer model to simulate the radiative transfer parameters. However, if the TIR hyperspectral remote-sensing data are to be widely used, there are some problems in the cost and accuracy of obtaining the atmospheric information. Compared with the emissivity and temperature retrieval of many existing solutions, the atmospheric correction of TIR hyperspectral remote sensing data is still not well solved. It is feasible to measure the atmospheric information by the instrument itself or retrieve the atmospheric information from the data itself. Comparatively speaking, it is more objective to measure the atmospheric information synchronously by the instrument itself [25]. In planned follow-up equipment development, we will devote part of our work to this aspect of research.

To summarize, ATHIS has the ability to carry out preliminary remote-sensing operational applications, but from the current instrument status, data-processing model, and frequency of experiments, the application of ATHIS is still in the early stage, and further application is needed to determine its deficiencies and improve its performance.

References

[1] J. Wang, Y. Wang, and C. Li, "Noise model of hyperspectral imaging system and influence on radiation sensitivity," *J. Remote Sens.*, vol. 14, no. 4, pp. 607–620, Aug. 2010.

[2] J. Wang, W. Xu, L. Yuan, Y. Lin, Z. He, and J. Liu, "Background radiation suppression of a thermal infrared hyperspectral imaging system," *J. Infrared Millimeter Waves*, vol. 29, no. 6, pp. 419–430, Dec. 2010.

[3] J. Wang *et al.*, "Status and prospect of thermal infrared hyperspectral imaging technology," *J. Infrared Millimeter Waves*, vol. 34, no. 1, pp. 51–59, Feb. 2015.

[4] J. A. Hackwell *et al.*, "LWIR/MWIR imaging hyperspectral sensor for airborne and ground-based remote sensing," in *Proc. SPIE 2819 Imag. Spectrometry II*, Denver, CO, USA, 1996, pp. 102–107.

[5] P. G. Lucey *et al.*, "AHI: An airborne long-wave infrared hyperspectral imager," in *Proc. SPIE 3431, Airborne Reconnaissance XXII*, San Diego, CA, USA, 1998, pp. 36–43.

[6] J. Shepanski and S. Sandor-LeahyP, "The NGST long wave hyperspectral imaging spectrometer: Sensor hardware and data processing," in *Proc. SPIE 6206, Infrared Technol. Appl. XXXII*, Orlando, FL, USA, 2006, pp. 62062B-1–62062B-12.

[7] D. W. Warren, R. H. Boucher, D. J. Gutierrez, E. R. Keim, and M. G. Sivjee, "MAKO: A high-performance, airborne imaging spectrometer for the long-wave infrared," in *Proc. SPIE 7812, Imag. Spectrometry XV*, San Diego, CA, USA, 2010, pp. 78120N-1–78120N-10.

[8] J. L. Hall *et al.*, "MAGI: A new high-performance airborne thermal-infrared imaging spectrometer for earth science applications," *IEEE Trans. Geosci. Remote Sens.*, vol. 53, no. 10, pp. 5447–5457, May 2015.

[9] C. Coudrain *et al.*, "SIELETERS, an airborne infrared dual-band spectro-imaging system for measurement of scene spectral signatures," *Opt. Express*, vol. 23, no. 12, pp. 16164–16176, Jun. 2015.

[10] W. R. Johnson *et al.*, "HyTES: Thermal imaging spectrometer development," in *Proc. Aerosp. Conf.*, Big Sky, MT, USA, 2011, pp. 1–8.

[11] S. Achal, J. E. McFee, T. Ivanco, and C. Anger, "A thermal infrared hyperspectral imager (tasi) for buried landmine detection," in *Proc. SPIE 6553, Detection Remediation Technol. Mines Minelike Targets XII*, Orlando, FL, USA, 2011, pp. 655316-1–655316-11.

[12] E. Puckrin *et al.*, "Airborne measurements in the infrared using FTIR-based imaging hyperspectral sensors," in *Proc. SPIE 7482, Electro-Opt. Remote Sens., Photon. Technol., Appl. III*, Berlin, Germany, 2009, pp. 73240R-1–73240R-12.

[13] L. Yuan *et al.*, "Optical design, laboratory test, and calibration of airborne long wave infrared imaging spectrometer," *Opt. Express*, vol. 25, no. 19, pp. 22440–22454, Sep. 2017.

[14] Q. Meng, S. Liu, C. Li, and J. Wang, "Effect of slit on energy received by pixel of thermal infrared hyperspectral imager," *Semicond. Optoelectron.*, vol. 40, no. 4, pp. 467–472, Aug. 2019.

[15] P. Li, Y. Li, Y. Fu, and H. Gong, "Effect of oversample superposition on MTF for long wave infrared camera," *J. Infrared Millimeter Waves*, vol. 25, no. 1, pp. 13–16, Feb. 2006.

[16] R. Zhang and G. Tian, "Determination of emissivity of objects at normal temperature," *Kexue Tongbao*, vol. 26, no. 5, pp. 297–300, May 1981.

[17] C. Salvaggio and C. J. Miller, "Methodologies and protocols for the collection of midwave and longwave infrared emissivity spectral using a portable field spectrometer," in *Proc. SPIE 4381 Algorithms Multispectral, Hyperspectral, Ultraspectral Imagery VII*, Orlando, FL, USA, 2001, pp. 539–548.

[18] J. Huang, S. Liu, X. Gao, Z. Yang, Q. Ni, and L. Wu, "Experimental study of the thermal infrared emissivity variation of loaded rock and its significance," *Remote Sens.*, vol. 10, no. 6, pp. 818-1–818-17, 2018.

[19] C. C. Borel, "Iterative retrieval of surface emissivity and temperature for a hyperspectral sensor," in *Proc. 1st JPL Workshop Remote Sens. Land Surf. Emissivity*, Pasadena, CA, USA, 1997, pp. 1–5.

[20] A. Berk, P. Conforti, R. Kennett, T. Perkins, F. Hawes, and J. van den Bosch, "MODTRAN6: A major upgrade of the MODTRAN radiative transfer code," in *Proc. SPIE 9088, Algorithms Technol. Multispectral, Hyperspectral, Ultraspectral Imagery XX*, Baltimore, MD, USA, 2014, pp. 90880H-1– 90880H-7.

[21] M. Kanamitsu *et al.*, "NCEP–DOE AMIP-II Reanalysis (R-2)," *Bull. Amer. Meteorol. Soc.*, vol. 83, no. 11, pp. 1631–1644, Jun. 2002.

[22] D. Gu, A. R. Gillespie, A. B. Kahle, and F. D. Palluconi, "Autonomous atmospheric compensation (AAC) of high resolution hyperspectral thermal infrared remote-sensing imagery," *IEEE Trans. Geosci. Remote Sens.*, vol. 38, no. 6, pp. 2557–2570, Nov. 2000.

[23] S. J. Young, B. Robert Johnson, and J. A. Hackwell, "An in-scene method for atmospheric compensation of thermal hyperspectral data," *J. Geophys. Res.: Atmos.*, vol. 107, no. D24, pp. ACH 14-1–ACH 14-20, Dec. 2002.

[24] M. Schlerf *et al.*, "A hyperspectral thermal infrared imaging instrument for natural resources applications," *Remote Sens.*, vol. 4, no. 12, pp. 3995–4009, Dec. 2012.

[25] C. Liu, H. Shao, F. Xie, C. Li, and J. Wang, "Atmospheric correction system for airborne thermal infrared imaging spectrometer: General design," in *Proc. 5th Symp. Novel Optoelectron. Detection Technol. Appl.*, Xi'an, China, 2019, pp. 110232R-1–110232R-10.

Feng Xie received the B.S. degree in electronic science and technology from the University of Science and Technology Beijing, Beijing, China, in 2000, and the Ph.D. degree in physical geography from Beijing Normal University, Beijing, China, in 2006.

He is currently an Associate Researcher with the Key Laboratory of Spatial Active Opto-Electronic Techniques, Shanghai Institute of Technical Physics, Chinese Academy of Sciences, Shanghai, China. His main research interests include data collection system of UAV airborne hyperspectral, LiDAR remote sensng system, and information mining.
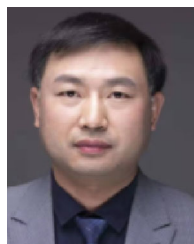
Jian Jin was born in China, in 1988. He received the B.S. degree in automation from Tianjin University, Tianjin, China, in 2011, and the M.S. degree in control engineering from Donghua University, Shanghai, China, in 2013.

He is currently an Research Assistant with the Key Laboratory of Spatial Active Opto-Electronic Techniques, Shanghai Institute of Technical Physics, Chinese Academy of Sciences, Shanghai, China. His current research interests include weak infrared spectrum signal processing and refrigeration infrared focal plane information acquisition.

Liyin Yuan was born in China, in 1981. She received the B.S. and Ph.D. degrees in optics from Tongji University, Shanghai, China, in 2003 and 2008, respectively.

She is currently an Associate Researcher with the Key Laboratory of Spatial Active Opto-Electronic Techniques, Shanghai Institute of Technical Physics, Chinese Academy of Sciences, Shanghai, China. Her current research interests include optical design, processing, installation, calibration, detection and other research work in infrared spectral imaging, and coded aperture snapshot spectral imaging.

Chengyu Liu was born in China, in 1985. He received the B.S. degree in GIS from Northeast Normal University, Changchun, China, in 2008, and the Ph.D. degree in natural resources from Beijing Normal University, Beijing, China, in 2013.

He is currently a Research Assistant with the Key Laboratory of Spatial Active Opto-Electronic Techniques, Shanghai Institute of Technical Physics, Chinese Academy of Sciences, Shanghai, China. His current interests include calibration and data processing of infrared hyperspectral remote sensing, water quality parameters, and sea ice parameters retrieval from hyperspectral remote sensing data.

Gang Lv was born in China, in 1980. He received the B.S. degree in mechanical engineering from Hefei Polytechnic University, Hefei, China, in 2002, and the M.S. degree in electronic science and technology from the Shanghai Institute of Technical Physics, Chinese Academy of Sciences, Shanghai, China, in 2011.

He is currently an Associate Researcher with the Key Laboratory of Spatial Active Opto-Electronic Techniques, Shanghai Institute of Technical Physics, Chinese Academy of Sciences. His current research interests include design of vacuum system and mechanical design of space photoelectric instrument.

Rui Xu was born in China, in 1986. He received the B.S. degree in electronic engineering and the Ph.D. degree in electronic science and technology from the University of Science and Technology of China, Hefei, China, in 2008 and 2013, respectively.

He is currently an Associate Researcher with the Key Laboratory of Spatial Active Opto-Electronic Techniques, Shanghai Institute of Technical Physics, Chinese Academy of Sciences, Shanghai, China. His current interests include calibration and data processing of infrared hyperspectral remote sensing.

Yueming Wang was born in China, in 1978. He received the B.S. degree in precision mechanical engineering from Tsinghua University, Beijing, China, in 2000, and the Ph.D. degree in electronic science and technology from the Shanghai Institute of Technical Physics, Chinese Academy of Sciences, Shanghai, China, in 2005.

He is currently a Researcher with the Key Laboratory of Spatial Active Opto-Electronic Techniques, Shanghai Institute of Technical Physics, Chinese Academy of Sciences. His current research interests include new hyperspectral fine spectroscopic technology, hyperspectral imaging system technology in aerospace, hyperspectral calibration and data preprocessing, and high-sensitivity infrared information acquisition technology.
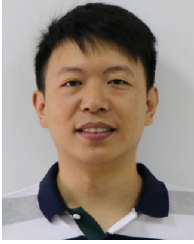
Chunlai Li was born in China, in 1982. He received the B.S. degree in optoelectronic engineering from the Huazhong University of Science and Technology, Wuhan, China, in 2004, and the Ph.D. degree in electronic science and technology from the Shanghai Institute of Technical Physics, Chinese Academy of Sciences, Shanghai, China, in 2009.

He is currently a Researcher with the Key Laboratory of Spatial Active Opto-Electronic Techniques, Shanghai Institute of Technical Physics, Chinese Academy of Sciences. His current research interests include weak infrared spectrum signal processing, refrigeration infrared focal plane information acquisition, and infrared hyperspectral data processing.

Jianyu Wang was born in China, in 1959. He received the B.S. degree in physics from Hangzhou University (now Zhejiang University), Hangzhou, China, in 1982, and the Ph.D. degree in physical electronics from the Shanghai Institute of Technical Physics, Chinese Academy of Sciences, Shanghai, China, 1990.

He is currently a Researcher with the Key Laboratory of Spatial Active Opto-Electronic Techniques, Shanghai Institute of Technical Physics, Chinese Academy of Sciences. His main research interests include free-space quantum communication and hyperspectral imaging system and application.

Dr. Wang was the member of COSBAR China Committee and the Academician with the Chinese Academy of Science.